Vibrational properties and thermal transport in quaternary chalcogenides: The case of Te-based compositions

Wencong Shi,[1] Tribhuwan Pandey,[2] Lucas Lindsay,[3] and Lilia M. Woods[1]
[1]*Department of Physics, University of South Florida, Tampa, Florida 33620, USA*
[2]*Department of Physics, University of Antwerp, B2020 Antwerp, Belgium*
[3]*Materials Science and Technology Division, Oak Ridge National Laboratory, Oak Ridge, Tennessee 37831, USA*

(Received 3 January 2021; accepted 16 March 2021; published 1 April 2021)

Vibrational thermal properties of $CuZn_2InTe_4$, $AgZn_2InTe_4$, and $Cu_2CdSnTe_4$, derived from binary II-VI zinc-blendes, are reported based on first-principles calculations. While the chalcogenide atoms in these materials have the same lattice positions, the cation atom arrangements vary, resulting in different crystal symmetries and subsequent properties. The compositional differences have important effects on the vibrational thermal characteristics of the studied materials, which demonstrate that low-frequency optical phonons hybridize with acoustic phonons and lead to enhanced phonon-phonon scattering and low lattice thermal conductivities. The phonon density of states, mode Grüneisen parameters, and phonon scattering rates are also calculated, enabling deeper insight into the microscopic thermal conduction processes in these materials. Compositional variations drive differences among the three materials considered here; nonetheless, their structural similarities and generally low thermal conductivities (0.5–4 W/m K at room temperature) suggest that other similar II-VI zinc-blende derived materials will also exhibit similarly low values, as also corroborated by experimental data. This, combined with the versatility in designing a variety of motifs on the overall structure, makes quaternary chalcogenides interesting for thermal management and energy conversion applications that require low thermal conductivity.

DOI: 10.1103/PhysRevMaterials.5.045401

I. INTRODUCTION

Multinary chalcogenides are a diverse group of materials with tunable electronic behaviors via a variety of possible dopants. This versatility has driven significant interest for both fundamental studies and practical applications [1,2]. For instance, chalcogenide glasses are mostly transparent from the visible to infrared spectrum and can be used in all-optical switching with suitable doping [3,4]. Some chalcogenides are also used as active catalysts in various chemical reactions [5]. The constituents of these materials are earth-abundant environmentally friendly compositions, which brings further benefit in commercial applications [6].

Multinary chalcogenides can be obtained from binary II-VI structures by a cross-cation substitution method [7], which gives rise to ternary and quaternary systems with varying properties [8–10]. Among the families of materials possible, the quaternary chalcogenides with chemical formula units I_2-II-IV-VI_4 and I-II_2-III-VI_4 (I = Cu or Ag; II = Zn or Cd; III = In, Ga, Al, or Tl; VI = S, Se, or Te) are especially interesting. They have similar structures and chemical stoichiometry, and the possibility to rearrange cations in different atomic sites gives many opportunities for fine property tuning.

The I_2-II-IV-VI_4 family of systems has been intensively investigated in the past several years due to their potential applications in photovoltaics and solar cells [11,12]. By properly choosing the cation atoms and doping configurations, one can achieve a 1.0–1.5 eV semiconducting energy gap, which is desirable for such applications [6–8,13,14]. Despite the sizable gap, the I_2-II-IV-VI_4 systems have also been shown to be attractive for thermoelectric applications. They have inherently low thermal conductivities, and with appropriate doping their energy gaps can be reduced [15,16]. On the other hand, researchers only recently began investigating the I-II_2-III-VI_4 family of materials. Experimental and theoretical studies have shown that $CuZn_2InSe_4$, $CuZn_2InTe_4$, $CuCd_2InTe_4$, $CuMn_2InTe_4$, and $AgZn_2InTe_4$ also have low thermal conductivities and varying electronic properties [17–20]. Additionally, first-principles simulations have given a comprehensive examination of the structural and electronic stabilities in terms of several possible lattice structures for this class of materials [21].

First-principles simulations have also shown that the remarkably low thermal conductivities in Cu_2ZnSnS_4 and $Cu_2ZnSnSe_4$ are directly related to the lattice structure and different phonon-phonon scattering channels limiting the phonon conduction processes [22,23]. However, no such investigations have been reported for representatives of the I-II_2-III-VI_4 class of materials.

In this work, we focus on the vibrational and thermal transport properties of $CuZn_2InTe_4$, $AgZn_2InTe_4$, and $Cu_2CdSnTe_4$. More specifically, lattice dynamical behaviors (e.g., dispersions, densities of states, and mode Grüneisen parameters) are calculated from density functional theory (DFT). These are then incorporated with quantum perturbation theory and the phonon Boltzmann transport equation to

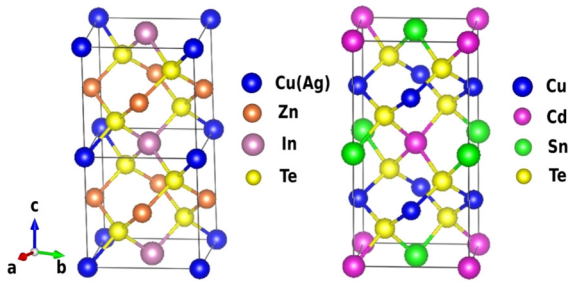

FIG. 1. Crystal structures for $Cu(Ag)Zn_2InTe_4$ (left) and $Cu_2CdSnTe_4$ (right). Two unit cells stacked along the c lattice direction for the $Cu(Ag)Zn_2InTe_4$ materials are shown for better comparison with the unit cell of the $Cu_2CdSnTe_4$ system.

determine thermal conductivities (κ_l) fully from first principles. These results give a representation of how vibrational characteristics change within structurally related Te-based I_2-II-IV-VI_4 and I-II_2-III-VI_4 quaternary chalcogenides of varying compositions.

II. CRYSTAL STRUCTURES

The $CuZn_2InTe_4$ and $AgZn_2InTe_4$ materials are synthesized in a modified zinc-blende structure, where the cations occupy the 4a $(0, 0, 0)$ Wyckoff sites and the chalcogen is found in the 4a $(0.25,\ 0.25,\ 0.25)$ Wyckoff position [17–19]. Though this lattice type (shown in Fig. 1) is similar to the standard zinc-blende structure with cubic symmetry, different chemical compositions give lower symmetry structures, and metallic atoms with varying sizes can lead to different lattice constants, straying from cubic, which is also found in our simulations (see Table I). The different lattice constants and the occupation of the 4a Wyckoff position by various cations determines this unique type-$P\bar{4}2m$ symmetry.

The $Cu_2CdSnTe_4$ material is experimentally reported in a stannite structure (shown in Fig. 1) [24], which belongs to the $I\bar{4}2m$ space group. This type of lattice is also zinc-blende derived; however, there is a layered-like atomic arrangement with alternating I-II and II-IV cations along the c-axis. As a result, the unit cell of the stannite system can be viewed as double the unit cell of the $Cu(Ag)Zn_2InTe_4$ materials. Comparing the two types of lattices from Fig. 1 shows that while the positions of the chalcogen atoms are the same in both, the atomic sites for the metallic atoms are different. As discussed in more detail below, this added complexity results in stronger phonon resistance and lower thermal conductivity, particularly along the lower symmetry axis, when compared with the $Cu(Ag)Zn_2InTe_4$ systems, similar to adding disorder.

III. METHOD OF CALCULATIONS

In this work, we utilize DFT simulations as implemented in the Vienna *ab-initio* simulation package (VASP), which relies on a projector-augmented-wave method with periodic boundary conditions and a plane-wave basis set [25,26]. Using VASP, the structural parameters and interatomic force constants (IFCs) are obtained within both the local density approximation (LDA) and the generalized gradient approximation (GGA) with the Perdew-Burke-Ernzerhof (PBE) functional [27]. Energy cutoff values were set to 1.3 times the largest default cutoff energy of the atoms in each structure (following VASP developer recommendations). Specifically, the cutoff for $Cu_2CdSnTe_4$ and $CuZn_2InTe_4$ is 384 eV and for $AuZn_2InTe_4$ it is 359 eV. Relaxation criteria were set for 10^{-5} eV total energy convergence and 10^{-4} eV/Å total forces convergence. Also, a $12 \times 12 \times 12$ k-mesh was chosen with the tetrahedron integration method and Blöchl corrections [28] for the initial electronic structure calculations. The relaxed lattice constants are shown in Table I. As expected, a, b, and c calculated via the LDA are smaller than those obtained via the GGA [29]. This often gives softer GGA phonons and lower κ_l than for LDA values, as discussed later.

For $CuZn_2InTe_4$, the a, b, and c lattice constants are practically the same within both approximations. The experimentally obtained constant [18–20] is the same in all directions and its value is bigger than the LDA and smaller than the GGA results. For $AgZn_2InTe_4$, the c parameter is slightly elongated compared with a and b, while experiments [27] indicate that all lattice constants are the same. For the $Cu_2CdSnTe_4$, $a = b \approx \frac{c}{2}$, with the LDA values being smaller and the GGA values being larger than the experimentally reported ones [27]. The experimentally reported lattice constants generally compare better with those from the LDA.

With the VASP results for the relaxed structures as a basis, the phonon band structures, phonon densities of states (PDOS), and mode Grüneisen parameters are obtained using the PHONOPY code based on supercell displacement techniques [30]. Extensive testing has shown that for many materials, calculated IFCs are robust against atomic displacements that are a relatively small fraction of the interatomic spacing [31,32], thus here we have used the default value 0.03 Å for this parameter. To determine the lattice thermal conductivity, the third-order anharmonic IFCs are calculated using PHONO3PY to obtain three-phonon interaction matrix elements [30,33]. For $CuZn_2InTe_4$ and $AgZn_2InTe_4$, $3 \times 3 \times 3$ supercells containing 216 atoms are constructed, while for $Cu_2CdSnTe_4$, $3 \times 3 \times 2$ supercells containing 288 atoms are constructed. The IFCs are obtained by numerical differentiation from forces determined by the VASP calculations with

TABLE I. Calculated and measured lattice parameters of the studied structures. The experimental values for $CuZn_2InTe_4$ and $AgZn_2InTe_4$ are taken from Refs. [19,20] and for $Cu_2CdSnTe_4$ they are taken from Ref. [24].

	a (Å)			b (Å)			c (Å)		
	LDA	PBE	Expt.	LDA	PBE	Expt.	LDA	PBE	Expt.
$CuZn_2InTe_4$	6.052	6.232	6.150	6.053	6.231	6.150	6.053	6.239	6.150
$AgZn_2InTe_4$	6.158	6.345	6.250	6.158	6.345	6.250	6.181	6.366	6.250
$Cu_2CdSnTe_4$	6.123	6.314	6.198	6.123	6.314	6.198	12.149	12.434	12.256

displaced atoms (0.03 Å) in the supercell. For the harmonic and anharmonic IFCs, translational invariance was enforced which improves low-frequency acoustic phonon behaviors. The long-ranged dipole-dipole interactions are also taken into account when constructing the dynamical matrices that determine the phonons by the method proposed in Ref. [34].

The lattice conductivity is calculated using the PHONO3PY package. This code relies on the full solution of the Peierls-Boltzmann transport equation, beyond the relaxation time approximation (RTA) [33], which tends to underestimate the lattice thermal conductivity [35]. The lattice conductivity is a tensor given by

$$\boldsymbol{\kappa}_l = \frac{1}{NV}\sum_{(\boldsymbol{q},j)} C_{(\boldsymbol{q},j)}\boldsymbol{v}_{(\boldsymbol{q},j)} \otimes \boldsymbol{v}_{(\boldsymbol{q},j)} \cdot \boldsymbol{\tau}_{(\boldsymbol{q},j)}, \tag{1}$$

where N is the number of points sampled in the first Brillouin zone, V is the volume of the unit cell, $\boldsymbol{q}$ is the wave vector, j is the polarization, and the summation goes over modes in the first Brillouin zone. The heat capacity for each phonon mode $(\boldsymbol{q}, j)$ with frequency $\omega_{(\boldsymbol{q},j)}$ is $C_{(\boldsymbol{q},j)} = k_B(\hbar\omega_{(\boldsymbol{q},j)}/k_BT)^2 \exp(\frac{\hbar\omega_{(\boldsymbol{q},j)}}{k_BT})/[\exp(\frac{\hbar\omega_{(\boldsymbol{q},j)}}{k_BT}) - 1]^2$. Note that $\boldsymbol{v}_{(\boldsymbol{q},j)} \otimes \boldsymbol{v}_{(\boldsymbol{q},j)}$ is a tensor product of the phonon group velocities defined as $\boldsymbol{v}_{(\boldsymbol{q},j)} = \nabla_{\boldsymbol{q}}\omega_{(\boldsymbol{q},j)}$. Only the diagonal components of $\boldsymbol{\kappa}_l$ are relevant for these systems.

The transport lifetimes $\boldsymbol{\tau}_{(\boldsymbol{q},j)}$ in Eq. (1) are built from the nonequilibrium distribution functions, which follow from solution of the Peierls-Boltzmann equation (Appendix E of Ref. [33]). The transport lifetimes depend on the direction of the applied gradient, unlike RTA lifetimes, $\tau^{\mathrm{RTA}}_{(\boldsymbol{q},j)} = 1/2\Gamma_{(\boldsymbol{q},j)}$, which are inversely related to the scattering rates or imaginary parts of the self-energies $\Gamma_{(\boldsymbol{q},j)}$ [e.g., Eq. (11) of Ref. [33]] [33,36–38]. The RTA tends to underestimate the phonon lifetimes and thus $\boldsymbol{\kappa}_l$, though in systems with strong umklapp scattering [39] relative to normal scattering these differences are not significant [35,37]. Both normal and umklapp processes are considered here [35,36]. The three-phonon scattering transition probabilities are determined from quantum perturbation theory. They enter the Peierls-Boltzmann equation and separately determine the self-energies [Eq. (11) of Ref. [33]]. These are a function of the harmonic (frequencies and eigenvectors) and anharmonic (matrix elements) IFCs. Phonon-isotope scattering associated with isotopic mass variations in the constituent atoms is also included in the calculations via quantum perturbation theory [40].

We find that $\boldsymbol{\kappa}_l$ values are well converged with $12 \times 12 \times 12$ k-meshes, thus in all cases we use $14 \times 14 \times 14$ k-meshes. Also, by testing anharmonic cutoff pair-distances in the range 3–9 Å for several cases, we find that the thermal conductivity values are not changed significantly for interaction distances larger than 6 Å. Therefore, to reduce the computational cost, all results for $\boldsymbol{\kappa}_l$ are obtained with a 6 Å pair-distance cutoff.

The Grüneisen parameter gives a measure of the anharmonicity in the interatomic bonds and is often correlated with the thermal conductivity [41]. Here we calculate mode Grüneisen parameters defined as $\gamma_{(\boldsymbol{q},i)} = -\frac{\partial \ln \omega_{(\boldsymbol{q},i)}}{\partial \ln V}$ for each phonon mode via numerical derivatives from phonon calculations at the equilibrium volume and two additional volumes that are slightly larger and smaller than the equilibrium value.

TABLE II. Calculated transverse acoustic and longitudinal acoustic speeds (m/s) along different directions in the Brillouin zones of the studied materials. These results correspond to the LDA phonon dispersions shown in Fig. 2.

	$AgZn_2InTe_4$			$CuZn_2InTe_4$			$Cu_2CdSnTe_4$		
	v_{TA1}	v_{TA2}	v_{LA}	v_{TA1}	v_{TA2}	v_{LA}	v_{TA1}	v_{TA2}	v_{LA}
$\Gamma - X$	2033	2051	3508	2244	2281	3661	2170	2170	2391
$\Gamma - M$	1839	2081	3579	1919	2295	3839			
$\Gamma - \Sigma$							1638	1791	3769
$\Gamma - Z$	2063	2063	3535	2287	2287	3691	1777	1777	3681

IV. RESULTS AND DISCUSSION

Recent experiments have shown that materials from the I_2-II-IV-VI_4 and I-II_2-III-VI_4 families have inherently low thermal conductivities. In particular, κ_l has been reported in the 0.5−3 W/m K range for several systems at room temperature [12,18–20,42]. These values are comparable to those of traditional thermoelectric materials [43–46] in which large average mass (m_{avg}) and strongly anharmonic bonds, often with complex atomic structures, have been identified as primary reasons for low κ_l. For example, PbTe ($m_{\mathrm{avg}} =$ 167.4 amu), Bi_2Te_3 ($m_{\mathrm{avg}} = 160.2$ amu), and $Yb_{14}MnSb_{11}$ ($m_{\mathrm{avg}} = 146.8$ amu), with κ_l values ranging from 0.8 to 2.4 W/m K [47–49]. Here, however, the average masses of $CuZn_2InTe_4$ ($m_{\mathrm{avg}} = 102.4$ amu), $AgZn_2InTe_4$ ($m_{\mathrm{avg}} =$ 108.0 amu), and $Cu_2CdSnTe_4$ ($m_{\mathrm{avg}} = 108.5$ amu) are relatively small (certainly smaller than the above-mentioned materials) and the lattice structure is not particularly complicated. *Ab initio* calculations will shed light on the microscopic origin of their unique vibrational properties to develop insights into their low lattice thermal conductivity values.

Calculated phonon dispersions for each material are presented in Fig. 2, which demonstrate the dynamical stability of each structure, i.e., no imaginary frequencies. A general contributing factor for low thermal conductivity is slow phonons, acoustic modes in particular. The calculated transverse-acoustic (TA) and longitudinal-acoustic (LA) low-frequency acoustic speeds (v_{TA} and v_{LA}, respectively) along characteristic directions in the Brillouin zones of the studied materials are shown in Table II. The acoustic velocities of the stannite material are generally smaller than those for the zinc-blende compositions. These sound speeds are comparable with those of Bi_2Te_3 ($v_{\mathrm{TA}} = 1870$ and 3390 m/s [50]) and PbTe ($v_{\mathrm{TA}} =$ 1210 m/s and $v_{\mathrm{LA}} = 3570$ m/s [51]) except perhaps the low v_{TA} for PbTe.

The partial densities of states (PDOS) corresponding to these dispersions are given in Fig. 3, which illustrates the relative importance of the different constituent atom vibrations in the varying frequency regions. In all cases, the Te atoms contribute about half of the total PDOS in the 1–2 THz range. The composite Te peak in the 3–4 THz region is also common to all materials. This, together with the strong cation-Te PDOS hybridization, can be traced to the atomic structures of the materials. The nearest-neighbor bonds are all formed between Te and metallic atoms, thus the abundance of Te is expected to have a significant impact on the entire phonon structure. It is also noted that the cation-Te nearest-neighbor

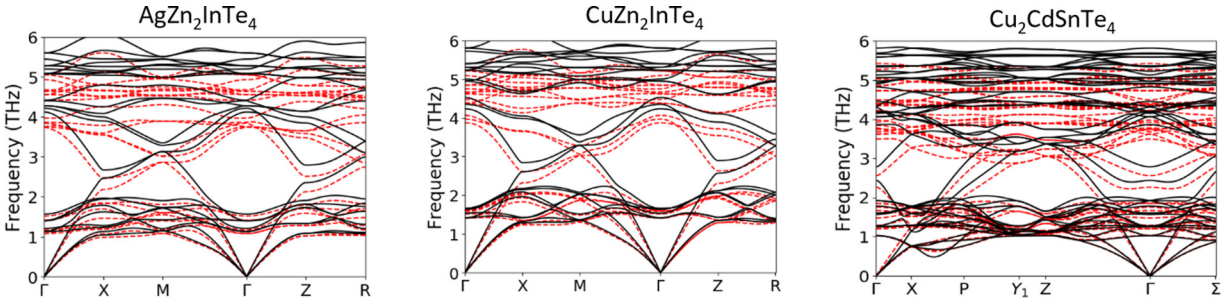

FIG. 2. LDA (black) and GGA (red) phonon dispersions for each material.

bonds are in the 2.69–2.84 Å range for $CuZn_2InTe_4$, 2.61–2.77 Å for $AgZn_2InTe_4$, and 2.52–2.78 Å for $Cu_2CdSnTe_4$. In general, bond lengths scale with the spring constants (k_0) that govern vibrational frequencies within classical models for which $\omega \sim \sqrt{k_0/m}$, where m is the mass. The similarity in the distance ranges and the fact that much of the vibrational behavior in all systems is governed by Te atoms are consistent with the overall similarity in range of frequencies among the materials. This is also consistent with their relatively similar sound speeds.

In addition to the acoustic modes (typical heat carriers in semiconducting materials), degrees of freedom associated with optical modes can be important in governing thermal conductivity via scattering resistance. Figure 2 shows that for all structures, a dense band of low-frequency optical phonons exists in the 1–2 THz range, with $Cu_2CdSnTe_4$ having the largest spread. These flat low-frequency bands disrupt the heat-carrying acoustic phonons and provide strong scattering channels for them. We also note that $Cu_2CdSnTe_4$ has twice the number of degrees of freedom as the other two systems, which thus provides acoustic phonons with many more scattering opportunities.

Each scattering transition is governed by the anharmonic coupling between the interacting phonons. The strength of this anharmonicity can be measured by the mode Grüneisen parameters $\gamma_{(\boldsymbol{q},j)}$, which we present in Fig. 3. The $\gamma_{(\boldsymbol{q},j)}$ have similar spectral characteristics for the studied materials. At low frequencies ($\omega < 2$ THz) the Grüneisen parameters are mostly negative, indicative of low-frequency mode hardening with volume expansion of the lattice. The frequency region $\omega \sim 2-3$ THz has a sparse positive distribution of $\gamma_{(\boldsymbol{q},j)}$, which correlates with the low PDOS in this region. For frequencies larger than 3 THz, the mode Grüneisen parameters lack dispersion having values 1–2 in all three materials, with $Cu_2CdSnTe_4$ having generally larger values signifying larger anharmonicity in this material. Thus, despite $Cu_2CdSnTe_4$ having similar sound speeds, dispersion frequency scale, and similar structure, we expect this material to have lower ther-

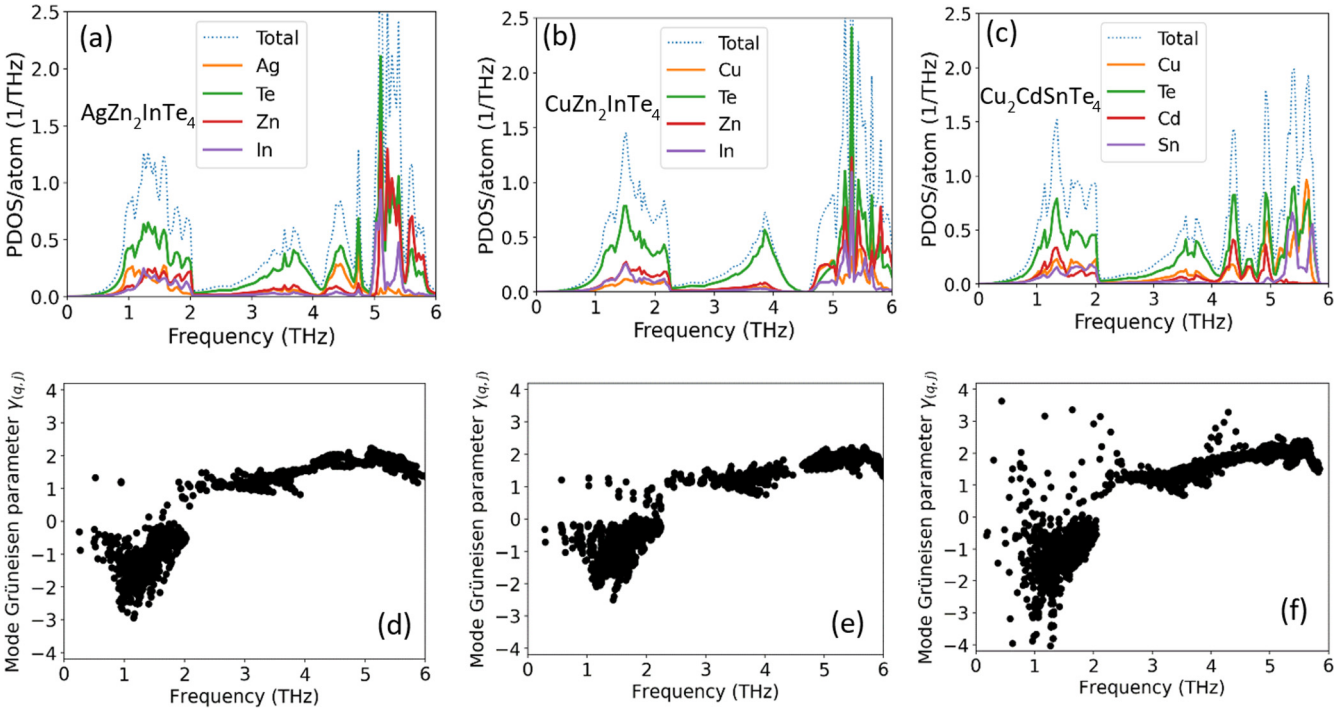

FIG. 3. Phonon density of states per atom for (a) $AgZn_2InTe_4$, (b) $CuZn_2InTe_4$, and (c) $Cu_2CdSnTe_4$. Mode Grüneisen parameters $\gamma_{(\boldsymbol{q},j)}$ for (d) $AgZn_2InTe_4$, (e) $CuZn_2InTe_4$, and (f) $Cu_2CdSnTe_4$. Results here are obtained within the LDA.

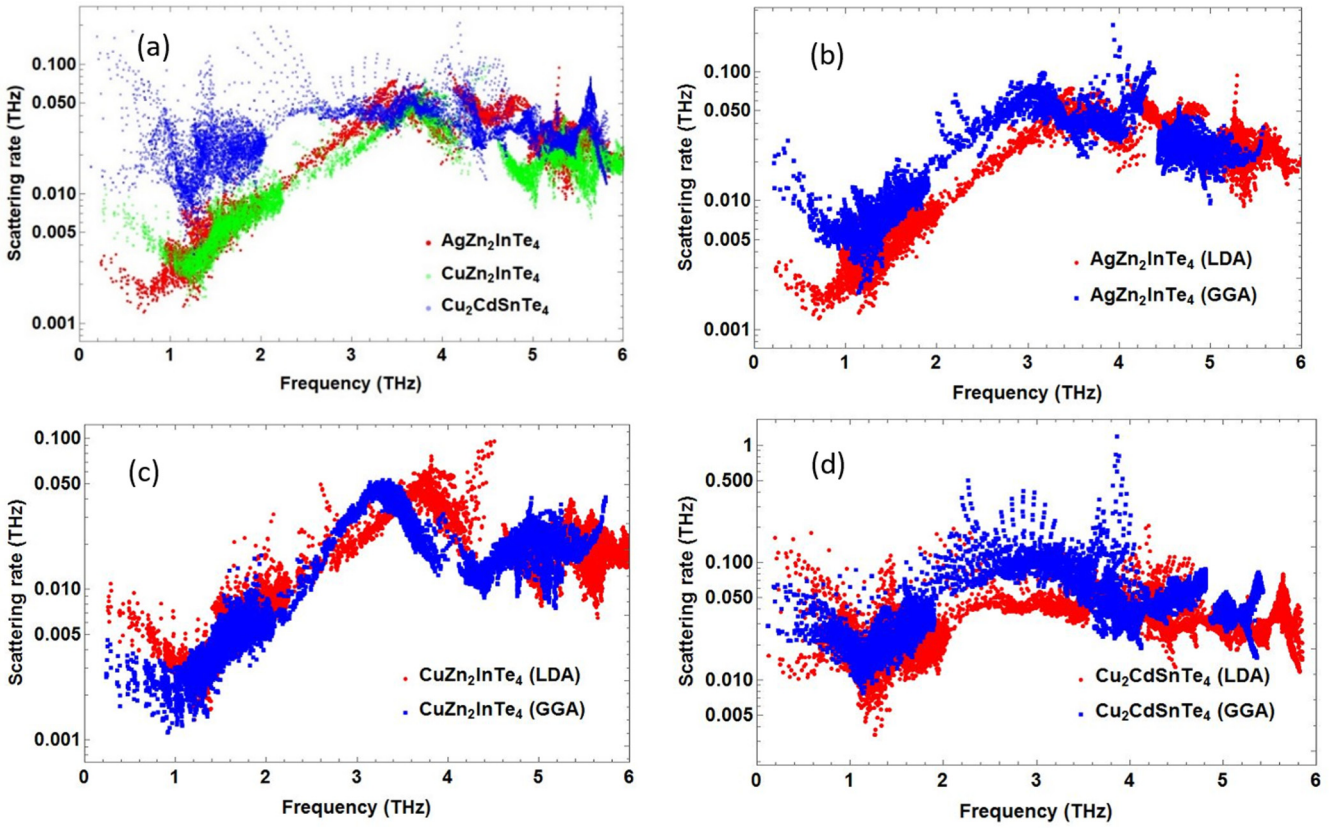

FIG. 4. (a) Room-temperature phonon scattering rates for the studied compositions obtained via the LDA. Comparison of the LDA and GGA phonon scattering rates for (b) $AgZn_2InTe_4$, (c) $CuZn_2InTe_4$, and (d) $Cu_2CdSnTe_4$.

mal conductivity due to its having more scattering channels, stronger anharmonicity, and more configurational complexity. Further insight can be gained from comparing the three-phonon RTA scattering rates $\Gamma_{(\boldsymbol{q},j)} = 1/2\tau^{\mathrm{RTA}}_{(\boldsymbol{q},j)}$ directly [see Fig. 4(a)]. Note that the transport lifetimes in Eq. (1) depend nontrivially on the distributions of all phonons, thus assigning individual "scattering rates" based on the inverse of the transport lifetimes is not appropriate. The largest low-frequency values (<3 THz) are found for $Cu_2CdSnTe_4$, in line with having more scattering channels and stronger anharmonicity. $AgZn_2InTe_4$ has the smallest scattering rates of these materials below 1 THz. Above 3 THz, all materials have similar scattering rates. We note that most of the heat is carried by phonons with frequencies less than 3 THz in these systems.

Again, the stronger phonon scattering in $Cu_2CdSnTe_4$ is related to having stronger lattice "disorder" in comparison with the other two materials. The alternating Cd and Sn arrangements (Cd in the corners and Sn in the center of the base of the unit cell followed by Cd in the center and Sn in the corners in the middle of the unit cell, as shown in Fig. 1) in two adjacent layers lead to essentially doubling the unit cell of the tetragonal stannite lattice as compared to the structure of $CuZn_2InTe_4$ and $AgZn_2InTe_4$. This will also be evident in the stronger transport anisotropy in $Cu_2CdSnTe_4$, as discussed below.

The calculated lattice thermal conductivity for each material as a function of temperature is presented in Fig. 5. The data are shown with regions shaded in different colors, corresponding to each material, and bound by results obtained from separate LDA and GGA calculations. At room temperature, the calculated LDA (GGA) κ_{xx} values are 3.78 (4.01), 3.21 (1.15), and 0.95 (0.53) W/m K for $CuZn_2InTe_4$, $AgZn_2InTe_4$, and $Cu_2CdSnTe_4$, respectively. These values are comparable with prominent thermoelectrics Bi_2Te_3, PbTe, and $Yb_{14}MnSb_{11}$ with room-temperature κ_l values ranging from 0.8 to 2.4 W/m K [47–49].

As GGA calculations tend to overestimate lattice constants while the LDA tends to underestimate them (see Table I), this drives weaker bonding and typically softer phonons in GGA calculations compared with those of the LDA. This generally gives smaller sound velocities and can lead to stronger scattering in GGA calculations depending on how the phase space for scattering varies as dictated by energy and momentum conservation conditions. Furthermore, weaker bonding often couples with stronger anharmonicity, though all these effects combine nontrivially to determine the thermal conductivity of a given material.

Indeed, LDA calculations give larger $\boldsymbol{\kappa}_l$ for $AgZn_2InTe_4$ and $Cu_2CdSnTe_4$. For $CuZn_2InTe_4$, GGA calculations yield higher $\boldsymbol{\kappa}_l$ due to the GGA also giving smaller scattering rates for phonons with frequencies below ∼1.5 THz, likely due to changes in the phase space for phonon scattering in this region. Nonetheless, GGA and LDA calculations are very similar for the two Cu-derived systems. On the other hand, the variation in thermal conductivity with DFT functional is quite large for the $AgZn_2InTe_4$ system. As shown in Fig. 4, the GGA scattering rates are significantly larger than those from the LDA, while the LDA and GGA rates are more

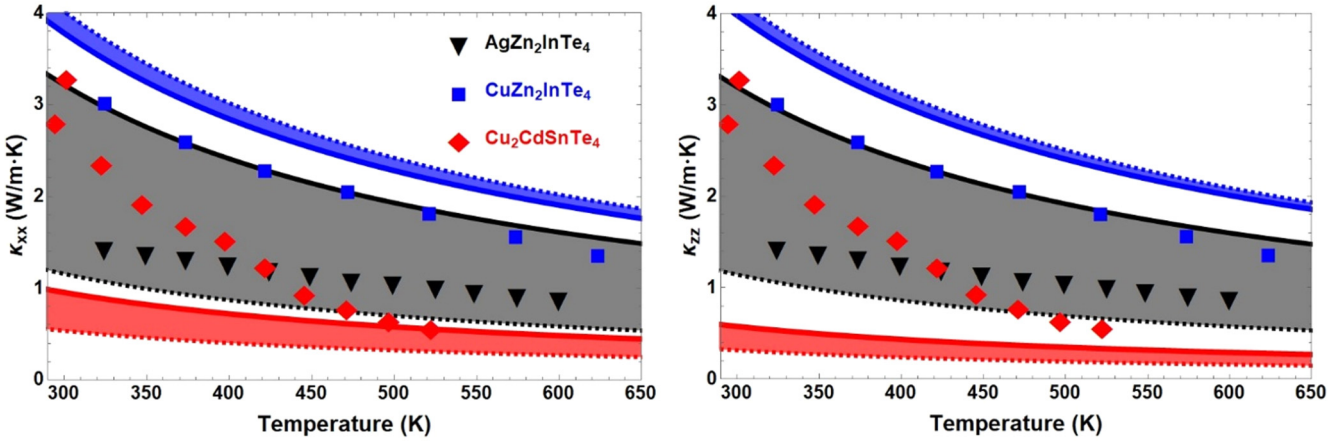

FIG. 5. Lattice thermal conductivity components (κ_{xx}, left panel; κ_{zz}, right panel) as a function of temperature. In each case, the shaded region is bound by κ_l obtained by LDA (solid curves) and GGA (dashed curves). The experimental values are given as discrete symbols [19,20,24]. The black, blue, and red curves correspond to $AgZn_2InTe_4$, $CuZn_2InTe_4$, and $Cu_2CdSnTe_4$, respectively.

similar in the other materials. The LDA and GGA dispersions are not significantly different in the frequency region $\omega < 3$ THz of the heat-carrying acoustic phonons. The main differences occur for higher-frequency optic branches from LDA calculations compared to those from GGA calculations, particularly for the highest-frequency branches, which is the case for all materials. By examining the LDA and GGA dispersions among the materials, it is not obvious that $AgZn_2InTe_4$ should have a significantly increased phase space for phonon scattering, thus differences may be driven by variations in anharmonicity. However, LDA and GGA calculated Grüneisen parameters for $AgZn_2InTe_4$ are also similar (not shown here), thus the origin for the κ_l differences is elusive [19,20,24]. We note that previous calculations comparing LDA and GGA phonon-mediated lattice thermal conductivities also found larger discrepancies for Ag compared with other elemental metallic systems [52]. We also note that Ag vibrations contribute strongly to the phonon DOS ~1 THz, unlike the metallic atom vibrational behaviors in the other systems.

Turning to $Cu_2CdSnTe_4$, as expected from the previous discussion, this system has the lowest calculated thermal conductivity and demonstrates more anisotropy. For example, at $T = 300$ K, LDA calculated values are $\kappa_{xx} = 0.95$ W/m K and $\kappa_{zz} = 0.58$ W/m K, while the lattice thermal conductivity is nearly isotropic for the other materials. This complexity-driven thermal behavior can be important in the design of better thermoelectric materials where reduced phonon conduction without significant reduction of electronic properties is desired. The κ_{zz} is lower than κ_{xx} in $Cu_2CdSnTe_4$ because the increased configurational complexity occurs along this direction. We note that $Cu_2CdSnTe_4$ is also semimetallic, while Ag(Cu)Zn_2InTe_4 are wider-band-gap semiconductors [19,20,24]. Though electronic contributions to the thermal conductivity and phonon resistivity are not considered here, this may be more important in this system.

The semimetallic nature of $Cu_2CdSnTe_4$ may also contribute to the strong discrepancy in temperature-dependent κ_l behavior when comparing calculations with measured data. Calculations give $\kappa_l \sim 1/T$ for all three materials in the temperature range considered in Fig. 5 ($300 < T < 650$ K), as expected for three-phonon dominated scattering in materials with relatively low Debye temperatures. This behavior is also generally observed for the measured κ_l data for (Ag)$CuZn_2InTe_4$ [19,20,24] with measured data just below the calculated curves for $CuZn_2InTe_4$ and sandwiched between LDA and GGA calculated curves for $AgZn_2InTe_4$. Note that calculations do not consider possible uncharacterized extrinsic scattering mechanisms, e.g., point defects, grain boundaries, etc., and thus they provide an upper estimate to κ_l. In this temperature range, we expect that boundary scattering resistance for realistic grain sizes is negligible for each system. For $Cu_2CdSnTe_4$, on the other hand, calculations and measurements agree at high temperature ($T < 500$ K), but the measured κ_l displays an unusual $T^{-2.9}$ dependence, while measured data below room temperature (not shown) are linearly decreasing with temperature. This unusual behavior is not captured within our current simulations and requires further investigation. Specifically, scattering mechanisms associated with point defects and grain boundaries, for example, are expected to be important at lower temperatures, thus they need to be included in future calculations for the $T < 300$ K temperature regime.

V. CONCLUSIONS

$CuZn_2InTe_4$, $AgZn_2InTe_4$, and $Cu_2CdSnTe_4$ are representatives of a large group of quaternary chalcogenide materials derivable from simpler binary II-VI zinc-blendes, which can accommodate many different cation atoms in their structures. The common origin and cation atom diversity, two somewhat counterintuitive trends, uniquely affect the transport in these materials, and first-principles simulations are indispensable in understanding their underlying mechanisms and structure-property relations.

Here we have studied the vibrational and thermal transport properties in $CuZn_2InTe_4$, $AgZn_2InTe_4$, and $Cu_2CdSnTe_4$ using *ab initio* methods. Two of the compositions, $CuZn_2InTe_4$ and $AgZn_2InTe_4$, have recently been synthesized and they belong to the relatively unexplored I-II_2-III-VI_4 class, while $Cu_2CdSnTe_4$ is synthesized with a stannite lattice and it

belongs to the I_2-II-IV-VI_4 family of materials. While most experimental and theoretical studies have focused on S- and Se-based kesterites from I_2-II-IV-VI_4, our study on Te-based systems is complementary to those reports and it broadens basic understanding of quaternary chalcogenides derived from II-VI zinc-blendes.

The atomic structure of $CuZn_2InTe_4$ and $AgZn_2InTe_4$ is relatively simple as it closely resembles the standard zinc-blende structure. The stannite $Cu_2CdSnTe_4$ is also similar, but because of the layered-like cation arrangement, the unit cell is twice as big as the one for $CuZn_2InTe_4$ and $AgZn_2InTe_4$, creating greater disorder along the z-direction. Despite their noncomplicated atomic structures and low average masses, we find their thermal conductivities to be relatively low. Similar values are also reported in recent experimental studies [19,20]. Our calculations rely on solving the phonon Boltzmann equation, in which the thermal transport is limited by three-phonon scattering mechanisms, which makes our results more suitable for room and higher temperatures.

We find that low-frequency optical phonons suppress the acoustic mode contributions in the $\omega < 3$ THz range, which is a key factor for increasing the phonon scattering phase space. The low thermal conductivity behavior is present not only in the $CuZn_2InTe_4$ and $AgZn_2InTe_4$ semiconductors, but also in the $Cu_2CdSnTe_4$ semimetal. Comparing our calculations with first-principles studies [22,23] on Cu_2ZnSnS_4 and $Cu_2ZnSnSe_4$ shows that low-frequency optical phonon hybridization with acoustic modes is key to the inherent anharmonicity in quaternary chalcogenides.

Our investigation suggests that low thermal conductivity is expected in quaternary chalcogenides despite their electronic properties. By selecting semiconducting compositions with greater disorder in the lattice due to cation atom arrangement, further reductions in κ_l may be achieved, which can be especially attractive for thermoelectric and thermal barrier applications.

ACKNOWLEDGMENTS

L.M.W. acknowledges financial support from the U.S. National Science Foundation under Grant No. DMR-1748188. L.L. acknowledges support for calculation guidance and manuscript development from the U.S. Department of Energy, Office of Science, Office of Basic Energy Sciences, Material Sciences and Engineering Division. Computational resources were provided by USF Research Computing and by the National Energy Research Scientific Computing Center (NERSC), a DOE Office of Science User Facility supported by the Office of Science of the U.S. Department of Energy under Contract No. DE-AC02-05CH11231.

The authors declare no competing financial interest.

[1] M. Kastner, Bonding Bands, Lone-Pair Bands, and Impurity States in Chalcogenide Semiconductors, Phys. Rev. Lett. **28**, 355 (1972).

[2] S. L. Li, K. Tsukagoshi, E. Orgiu, and P. Samorì, Charge transport and mobility engineering in two-dimensional transition metal chalcogenide semiconductors, Chem. Soc. Rev. **45**, 151 (2016).

[3] B. Bureau, X. H. Zhang, F. Smektala, J. L. Adam, J. Troles, H. L. Ma, C. Boussard-Plèdel, J. Lucas, P. Lucas, D. Le Coq, M. R. Riley, and J. H. Simmons, Recent advances in chalcogenide glasses, J. Non. Cryst. Solids. **345–346**, 276 (2004).

[4] A. Zakery and S. R. Elliott, Optical properties and applications of chalcogenide glasses: A review, J. Non. Cryst. Solids **330**, 1 (2003).

[5] G. Liu, H. Zhang, and J. Hu, Novel synthesis of a highly active carbon-supported Ru85Se15 chalcogenide catalyst for the oxygen reduction reaction, Electrochem. Commun. **9**, 2643 (2007).

[6] S. Adachi, *Earth-Abundant Materials for Solar Cells: Cu2-II-IV-VI4 Semiconductors* (John Wiley & Sons, Inc., Chichester, UK, 2015).

[7] C. H. L. Goodman, The prediction of semiconducting properties in inorganic compounds, J. Phys. Chem. Solids **6**, 305 (1958).

[8] S. Chen, X. G. Gong, A. Walsh, and S.-H. Wei, Electronic structure and stability of quaternary chalcogenide semiconductors derived from cation cross-substitution of II-VI and I-III-VI 2 compounds, Phys. Rev. B **79**, 165211 (2009).

[9] S. Chen, A. Walsh, Y. Luo, J.-H. Yang, X. G. Gong, and S.-H. Wei, Wurtzite-derived polytypes of kesterite and stannite quaternary chalcogenide semiconductors, Phys. Rev. B **82**, 195203 (2010).

[10] C. Wang, S. Chen, J.-H. Yang, L. Lang, H.-J. Xiang, X.-G. Gong, A. Walsh, and S.-H. Wei, Design of I_2–II–IV–VI_4 semiconductors through element substitution: The thermodynamic stability limit and chemical trend, Chem. Mater. **26**, 3411 (2014).

[11] D. A. R. Barkhouse, O. Gunawan, T. Gokmen, T. K. Todorov, and D. B. Mitzi, Device characteristics of a 10.1% hydrazine-processed $Cu_2ZnSn(Se, S)_4$ solar cell, Prog. Photovoltaics Res. Appl. **20**, 6 (2012).

[12] M. Ibáñez, R. Zamani, A. LaLonde, D. Cadavid, W. Li, A. Shavel, J. Arbiol, J. R. Morante, S. Gorsse, G. J. Snyder, and A. Cabot, $Cu_2ZnGeSe_4$ nanocrystals: Synthesis and thermoelectric properties, J. Am. Chem. Soc. **134**, 4060 (2012).

[13] T. Jing, Y. Dai, X. Ma, W. Wei, and B. Huang, Electronic structure and photocatalytic water-splitting properties of $Ag_2ZnSn(S_1 - xSex)_4$, J. Phys. Chem. C **119**, 27900 (2015).

[14] A. Ghosh, S. Palchoudhury, R. Thangavel, Z. Zhou, N. Naghibolashrafi, K. Ramasamy, and A. Gupta, A new family of wurtzite-phase Cu_2ZnAS_{4-x} and $CuZn_2AS_4$ (A = Al, Ga, In) nanocrystals for solar energy conversion applications, Chem. Commun. **52**, 264 (2016).

[15] P. Qiu, X. Shi, and L. Chen, Cu-based thermoelectric materials, Energy Storage Mater. **3**, 85 (2016).

[16] A. V. Powell, Recent developments in Earth-abundant copper-sulfide thermoelectric materials, J. Appl. Phys. **126**, 100901 (2019).

[17] D. Hobbis, W. Shi, A. Popescu, K. Wei, R. E. Baumbach, H. Wang, L. M. Woods, and G. S. Nolas, Synthesis, transport properties and electronic structure of p-type $Cu_{1+x}Mn_{2-x}InTe_4$ (x = 0, 0.2, 0.3), Dalt. Trans. **49**, 2273 (2020).

[18] W. Shi, A. R. Khabibullin, D. Hobbis, G. S. Nolas, and L. M. Woods, Electronic structure properties of $CuZn_2InTe_4$ and $AgZn_2InTe_4$ quaternary chalcogenides, J. Appl. Phys. **125**, 155101 (2019).

[19] D. Hobbis, K. Wei, H. Wang, and G. S. Nolas, Synthesis and transport properties of Cu-excess $Cu(Zn, Cd)_2InTe_4$ quaternary chalcogenides, J. Alloys Compd. **743**, 543 (2018).

[20] G. S. Nolas, M. S. Hassan, Y. Dong, and J. Martin, Synthesis, crystal structure and electrical properties of the tetrahedral quaternary chalcogenides CuM_2InTe_4 (M=Zn, Cd), J. Solid State Chem. **242**, 50 (2016).

[21] W. Shi, A. R. Khabibullin, and L. M. Woods, Exploring phase stability and properties of I-II_2-III-VI_4 quaternary chalcogenides, Adv. Theor. Simul. **3**, 2000041 (2020).

[22] T. Gürel, C. Sevik, and T. Çağın, Characterization of vibrational and mechanical properties of quaternary compounds Cu_2ZnSnS_4 and $Cu_2ZnSnSe_4$ in kesterite and stannite structures, Phys. Rev. B **84**, 205201 (2011).

[23] J. M. Skelton, A. J. Jackson, M. Dimitrievska, S. K. Wallace, and A. Walsh, Vibrational spectra and lattice thermal conductivity of kesterite-structured Cu_2ZnSnS_4 and $Cu_2ZnSnSe_4$, APL Mater. **3**, 041102 (2015).

[24] Y. Dong, A. R. Khabibullin, K. Wei, Z.-H. Ge, J. Martin, J. R. Salvador, L. M. Woods, and G. S. Nolas, Synthesis, transport properties, and electronic structure of $Cu_2CdSnTe_4$, Appl. Phys. Lett. **104**, 252107 (2014).

[25] G. Kresse and J. Furthmüller, Efficiency of ab-initio total energy calculations for metals and semiconductors using a plane-wave basis set, Comput. Mater. Sci. **6**, 15 (1996).

[26] G. Kresse and J. Furthmüller, Efficient iterative schemes for *ab initio* total-energy calculations using a plane-wave basis set, Phys. Rev. B **54**, 11169 (1996).

[27] J. P. Perdew, K. Burke, and M. Ernzerhof, Generalized Gradient Approximation Made Simple, Phys. Rev. Lett. **77**, 3865 (1996).

[28] P. E. Blöchl, O. Jepsen, and O. K. Andersen, Improved tetrahedron method for Brillouin-zone integrations, Phys. Rev. B **49**, 16223 (1994).

[29] P. Haas, F. Tran, and P. Blaha, Calculation of the lattice constant of solids with semilocal functionals, Phys. Rev. B **79**, 085104 (2009).

[30] A. Togo and I. Tanaka, First principles phonon calculations in materials science, Scr. Mater. **108**, 1 (2015).

[31] A. J. H. McGaughey, A. Jain, H. Y. Kim, and B. Fu, Phonon properties and thermal conductivity from first principles, lattice dynamics, and the Boltzmann transport equation, J. Appl. Phys. **125**, 011101 (2019).

[32] L. Lindsay and C. A. Polanco, Thermal transport by first-principles anharmonic lattice dynamics, in *Handbook of Materials Modeling*, edited by W. Andreoni and S. Yip (Springer, Cham, 2020), pp. 735–765.

[33] A. Togo, L. Chaput, and I. Tanaka, Distributions of phonon lifetimes in Brillouin zones, Phys. Rev. B **91**, 094306 (2015).

[34] X. Gonze and C. Lee, Dynamical matrices, Born effective charges, dielectric permittivity tensors, and interatomic force constants from density-functional perturbation theory, Phys. Rev. B **55**, 10355 (1997).

[35] L. Lindsay, First principles Peierls-Boltzmann phonon thermal transport: A topical review, Nanoscale Microscale Thermophys. Eng. **20**, 67 (2016).

[36] R. E. Peierls, *Quantum Theory of Solids* (Oxford University Press, London, 1995).

[37] A. A. Maradudin and A. E. Fein, Scattering of neutrons by an anharmonic crystal, Phys. Rev. **128**, 2589 (1962).

[38] L. Chaput, A. Togo, I. Tanaka, and G. Hug, Phonon-phonon interactions in transition metals, Phys. Rev. B **84**, 094302 (2011).

[39] K. Mizokami, A. Togo, and I. Tanaka, Lattice thermal conductivities of two SiO_2 polymorphs by first-principles calculations and the phonon Boltzmann transport equation, Phys. Rev. B **97**, 224306 (2018).

[40] S. I. Tamura, Isotope scattering of dispersive phonons in Ge, Phys. Rev. B **27**, 858 (1983).

[41] E. Grüneisen, Theorie des festen zustandes einatomiger elemente, Ann. Phys. **344**, 257 (1912).

[42] W. G. Zeier, Y. Pei, G. Pomrehn, T. Day, N. Heinz, C. P. Heinrich, G. J. Snyder, and W. Tremel, Phonon scattering through a local anisotropic structural disorder in the thermoelectric solid solution $Cu_2Zn_1 - xFexGeSe_4$, J. Am. Chem. Soc. **135**, 726 (2013).

[43] K. Biswas, J. He, I. D. Blum, C.-I. Wu, T. P. Hogan, D. N. Seidman, V. P. Dravid, and M. G. Kanatzidis, High-performance bulk thermoelectrics with all-scale hierarchical architectures, Nature (London) **489**, 411 (2012).

[44] E. S. Toberer, C. A. Cox, S. R. Brown, T. Ikeda, A. F. May, S. M. Kauzlarich, and J. G. Snyder, Traversing the metal-insulator transition in a zintl phase: Rational enhancement of thermoelectric efficiency in $Yb_{14}Mn_{1-x}Al_xSb_{11}$, Adv. Funct. Mater. **18**, 2795 (2008).

[45] J. He, M. G. Kanatzidis, and V. P. Dravid, High performance bulk thermoelectrics via a panoscopic approach, Mater. Today **16**, 166 (2013).

[46] S. K. Bux, J. P. Fleurial, and R. B. Kaner, Nanostructured materials for thermoelectric applications, Chem. Commun. **46**, 8311 (2010).

[47] C. B. Satterthwaite and R. W. Ure, Electrical and thermal properties of Bi_2Te_3, Phys. Rev. **108**, 1164 (1957).

[48] E. D. Devyatkova and I. A. Smirnov, The effect of halogen additions on the thermal conductivity of lead telluride, Sov. Phys.-Solid State **3**, 1666 (1962).

[49] S. R. Brown, S. M. Kauzlarich, F. Gascoin, and J. G. Snyder, $Yb_{14}MnSb_{11}$: New high efficiency thermoelectric material for power generation, Chem. Mater. **18**, 1873 (2006).

[50] X. Gao, M. Zhou, Y. Cheng, and G. Ji, First-principles study of structural, elastic, electronic and thermodynamic properties of topological insulator Bi_2Se_3 under pressure, Philos. Mag. **96**, 208 (2016).

[51] Y. Amouyal, A practical approach to evaluate lattice thermal conductivity in two-phase thermoelectric alloys for energy applications, Materials (Basel) **10**, 386 (2017).

[52] Y. Wang, Z. Lu, and X. Ruan, First principles calculation of lattice thermal conductivity of metals considering phonon-phonon and phonon-electron scattering, J. Appl. Phys. **119**, 225109 (2016).